



University of  
Massachusetts  
Amherst

## Floating Platform Effects on Power Generation in Spar and Semisubmersible Wind Turbines

Item Type	Article
Authors	Johlas, Hannah M.;Martínez-Tossas, Luis A.;Churchfield, Matthew J.;Lackner, Matthew A.;Schmidt, David P.
DOI	<a href="https://doi.org/10.1002/we.2608">10.1002/we.2608</a>
Rights	Attribution-NonCommercial-NoDerivatives 4.0 International;UMass Amherst Open Access Policy
Download date	2026-04-10 22:48:55
Item License	<a href="http://creativecommons.org/licenses/by-nc-nd/4.0/">http://creativecommons.org/licenses/by-nc-nd/4.0/</a>
Link to Item	<a href="https://hdl.handle.net/20.500.14394/35739">https://hdl.handle.net/20.500.14394/35739</a>

## RESEARCH ARTICLE

WILEY

# Floating platform effects on power generation in spar and semisubmersible wind turbines

Hannah M. Johlas<sup>1</sup> | Luis A. Martínez-Tossas<sup>2</sup> | Matthew J. Churchfield<sup>2</sup> |  
Matthew A. Lackner<sup>1</sup> | David P. Schmidt<sup>1</sup>

<sup>1</sup>Department of Mechanical and Industrial Engineering, University of Massachusetts Amherst, Amherst, Massachusetts, USA

<sup>2</sup>National Wind Technology Center, National Renewable Energy Laboratory, Golden, Colorado, United States

## Correspondence

Hannah M. Johlas, Department of Mechanical and Industrial Engineering, University of Massachusetts Amherst, Amherst, MA, USA.  
Email: hjohlas@umass.edu

## Funding information

National Science Foundation, Grant/Award Numbers: 1451512, ACI-1548562

## Abstract

The design and financing of commercial-scale floating offshore wind projects require a better understanding of how power generation differs between newer floating turbines and well-established fixed-bottom turbines. In floating turbines, platform mobility causes additional rotor motion that can change the time-averaged power generation. In this work, OpenFAST simulations examine the power generated by the National Renewable Energy Laboratory's 5-MW reference turbine mounted on the OC3-UMaine spar and OC4-DeepCWind semisubmersible floating platforms, subjected to extreme irregular waves and below-rated turbulent inflow wind from large-eddy simulations of a neutral atmospheric boundary layer. For these below-rated conditions, average power generation in floating turbines is most affected by two types of turbine displacements: an average rotor pitch angle that reduces power, caused by platform pitch; and rotor motion upwind-downwind that increases power, caused by platform surge and pitch. The relative balance between these two effects determines whether a floating platform causes power gains or losses compared to a fixed-bottom turbine; for example, the spar creates modest (3.1%–4.5%) power gains, whereas the semisubmersible creates insignificant (0.1%–0.2%) power gains for the simulated conditions. Furthermore, platform surge and pitch motions must be analyzed concurrently to fully capture power generation in floating turbines, which is not yet universal practice. Finally, a simple analytical model for predicting average power in floating turbines under below-rated wind speeds is proposed, incorporating effects from both the time-averaged pitch displacement and the dynamic upwind-downwind displacements.

## KEYWORDS

floating wind turbine, large-eddy simulation, power generation, semisubmersible, spar

## 1 | INTRODUCTION

Floating offshore wind turbines are an emerging technology in the global wind energy market, with several multiturbine floating pilot projects already installed and the first large-scale floating projects expected within the decade.<sup>1</sup> As offshore wind energy moves into deeper waters

[Correction added on 4 March 2021, after first online publication: URL for peer review history has been corrected.]

This is an open access article under the terms of the Creative Commons Attribution-NonCommercial-NoDerivs License, which permits use and distribution in any medium, provided the original work is properly cited, the use is non-commercial and no modifications or adaptations are made.

© 2021 The Authors. Wind Energy published by John Wiley & Sons Ltd.

beyond 50- to 60-m depth to access higher wind resources and new energy markets, floating platforms become more economical than fixed-bottom options.<sup>2,3</sup> Floating turbines offer unique engineering challenges due to the coupling of platform mobility to aerodynamic loads on the turbine rotor. Aerodynamic and hydrodynamic loadings cause platform and therefore rotor displacements, changing the relative wind at the rotor, which in turn affects the aerodynamic loads on the rotor. This coupling affects the power generation, structural loads, and wind flow around the turbine.<sup>4,5</sup> Accurately predicting the power generation for floating turbines is vital for designing and financing large-scale floating wind projects. In particular, it is important to understand how and why power generation differs between floating turbines and fixed-bottom turbines, so that appropriate adjustments can be made to power prediction models used in project design and planning.

Floating platform displacements are described by 6 degrees of freedom: surge, sway, heave, pitch, roll, and yaw, as illustrated in Figure 1. These platform displacements cause displacements of the rotor, also shown in Figure 1: the three linear displacements of the rotor center,  $x_{rc}$ ,  $y_{rc}$ , and  $z_{rc}$ , as well as the rotor “pitch” and “yaw” angles due to platform displacements,  $\phi_{rc}$  and  $\theta_{rc}$ . In general, both rotor and platform displacements may include both fluctuating motions (“dynamic displacements”) and nonzero time-averaged positions (“time-averaged displacements”).

Previous studies examine how specific types of dynamic platform displacements affect a floating turbine's power generation. In particular, dynamic motions in surge and pitch typically increase time-averaged power generation: The associated rotor motions upwind-downwind change the relative wind speed experienced by the rotor, which results in a power gain when averaged over time. This phenomenon is observed for isolated pitch motions, isolated surge motions, and combinations of surge and pitch motions in various studies by Huang et al.,<sup>6</sup> Karimian Aliabadi and Rasekh,<sup>7</sup> Lin et al.,<sup>8</sup> Sant et al.,<sup>9</sup> Shen et al.,<sup>10</sup> and Wen et al.<sup>11-13</sup>

Other studies also document that statically angling the rotor relative to the wind decreases power generation. Specifically, static rotor yaw reduces a turbine's power generation,<sup>14,15</sup> with a power loss coefficient typically predicted by a  $\cos^n$  model.<sup>15</sup> Similarly, static rotor tilt decreases a turbine's power generation.<sup>14</sup> For floating turbines, platform yaw and pitch directly cause an angled rotor, which may act like static rotor yaw or tilt and decrease power.<sup>6</sup> Additionally, platform roll and heave may affect power by causing vertical rotor displacements within the wind shear profile, though the vertical displacements may be too small relative to the wind shear to create a substantial effect.

Although platform displacements are the underlying reason behind power gains or losses in floating turbines, previous studies rarely use representative displacement values. A realistic floating turbine's platform displacements are driven by stochastic environmental loads from irregular waves and turbulent wind, with possible coupling between different platform degrees of freedom.<sup>16</sup> Despite this, simulated platform displacement time histories are often approximated as prescribed sinusoids with time-averaged values of 0, and individual platform degrees of freedom are often studied in isolation.<sup>7,10-13,17,18</sup> Direct comparisons between multiple common floating platform types are also rare, limiting the ability to generalize trends across platform types. Notable exceptions include the work of Sebastian et al.,<sup>16</sup> which examined barge, spar, and tension-leg platforms with dynamic behavior under irregular waves and steady wind, and the work of Huang et al.,<sup>6</sup> which examined a spar platform with dynamic behavior under regular waves and steady wind.

This study aims to provide upper estimates for power gains or losses due to floating platform displacements for two common floating platform types, the spar and semisubmersible. Furthermore, this research seeks to link these power gains or losses to rotor displacement patterns and, in doing so, identify the underlying physical phenomena that cause differences in average power between floating and fixed-bottom turbines.

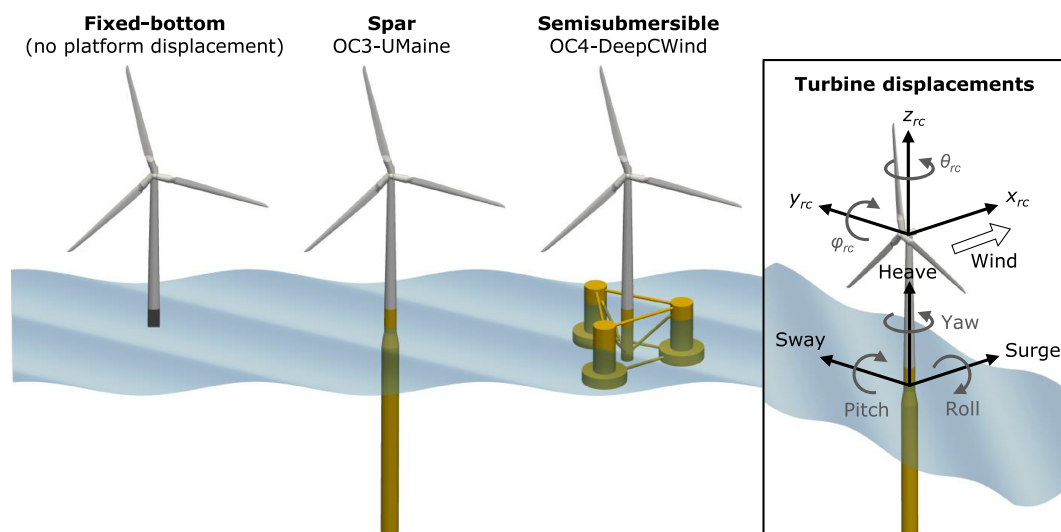


**FIGURE 1** The NREL 5-MW reference turbine mounted on a fixed-bottom platform (left), the OC3-UMaine/OC3-Hywind spar (center), and the OC4-DeepCWind semisubmersible (right). The subfigure on the right defines platform displacements (surge, sway, heave, pitch, roll, and yaw) as well as rotor displacements ( $x_{rc}$ ,  $y_{rc}$ ,  $z_{rc}$ ,  $\phi_{rc}$ , and  $\theta_{rc}$ )

Specifically, this study focuses on determining which types of realistic platform behavior most affect the average power for below-rated conditions, by addressing the following questions:

- Do any dynamic rotor and platform displacements significantly affect power?
- Do any time-averaged rotor and platform displacements significantly affect power?
- Which rotor and platform degrees of freedom affect power the most?
- How does average power generation differ between spar and semisubmersible platforms?

To answer these questions, floating wind turbines are simulated using two wind energy modeling tools developed by the National Renewable Energy Laboratory (NREL): OpenFAST<sup>19</sup> and the Simulator fOr Wind Farm Applications (SOWFA).<sup>20</sup> Section 2 describes the simulation setup, including details on the platform types, environmental conditions, simulation models, and case descriptions. Section 3 presents the simulated results for platform displacements, rotor displacements, and average power generation. In Section 4, a new analytical model for floating power generation is proposed and evaluated against the simulated results. Finally, Section 5 presents this study's conclusions about how specific turbine displacements affect average power generation in floating wind turbines.

## 2 | SIMULATION SETUP

### 2.1 | Platform types

This study simulates the power generation of the NREL 5-MW reference turbine, which has a diameter of  $D = 126$  m, a hub height of  $z_H = 90$  m, a rated wind speed of 11.4 m/s, and a shaft tilt of  $\phi_t = 5^\circ$ .<sup>21</sup> The simulated turbine is mounted on two floating platforms: the OC3-UMaine spar<sup>22</sup> and the OC4-DeepCWind semisubmersible.<sup>23</sup> The OC3-UMaine spar is identical to the OC3-Hywind spar,<sup>24</sup> except that the catenary mooring lines are adjusted to match the semisubmersible water depth of 200 m.<sup>22</sup> For comparison, a fixed-bottom version of the NREL 5-MW turbine is also replicated by disabling all platform displacements for a spar simulation. Figure 1 illustrates these three platform types: fixed-bottom, spar, and semisubmersible.

### 2.2 | Environmental conditions

This study considers the power generation under one combination of environmental conditions. The turbulent wind conditions represent an offshore atmospheric boundary layer with neutral stability, capped by a stable inversion at an elevation of 750 m. At hub height, the wind speed is 8 m/s and the turbulence intensity is 4%, with a wind shear of 0.008 m/s/m and a wind veer of  $0.02^\circ/\text{m}$  across the rotor height. Additional characteristics of a similar neutral boundary layer are described in the authors' previous work.<sup>25,26</sup> This 8-m/s wind speed is in the turbine's below-rated operating region, where tip-speed ratios are high and power generation is most influenced by platform behavior.<sup>7,8</sup>

The wave conditions are irregular, unidirectional JONSWAP waves in a water depth of 200 m. The irregular waves have a significant wave height of  $H_s = 8$  m and a peak spectral period of  $T_p = 14$  s. The wave propagation direction is aligned with the hub-height wind direction. These environmental conditions represent an unusual combination of below-rated wind speeds and very large waves; a more typical 10-year significant wave height might be 4.5–5 m for this wind speed.<sup>27</sup> Previous studies indicate that this combination increases the platform displacements<sup>25,27</sup> while remaining in the below-rated control regime where power is most affected by platform motions, therefore giving an upper estimate for the power gains or losses due to floating platform displacements.

### 2.3 | Simulation models

The spar, semisubmersible, and fixed-bottom turbines in these environmental conditions are simulated using OpenFAST v2.3.0,<sup>19</sup> NREL's modular aeroelastic engineering tool that models the platform motion, rotor motion, rotor aerodynamic performance, and power generation. Variable-speed control and blade-pitch control are included using OpenFAST's ServoDyn module, but the blade pitch remains at  $0^\circ$  due to the below-rated wind speed. The HydroDyn module models the irregular wave conditions. The turbulent inflow wind is generated by a large-eddy simulation of the atmospheric boundary layer flow. This large-eddy simulation is performed with SOWFA,<sup>20</sup> NREL's computational fluid dynamics tool based on OpenFOAM v2.4, which models the wind flow around the turbine.

The majority of the OpenFAST simulations in this study use a prerecorded time history of the inflow wind field. This prerecorded inflow is generated by sampling on a plane in the SOWFA large-eddy simulation, producing a time series of 2-D slices of the instantaneous wind field at

16 Hz. These slices are then converted to HAWC-format binary files and marched past the turbine in OpenFAST to recreate the SOWFA flow field time history at the rotor plane. This approach of using prerecorded SOWFA slices as inflow wind to a stand-alone OpenFAST simulation is documented further by Lee et al.<sup>28</sup>

Although computationally efficient, this prerecorded inflow field does not fully capture the two-way interaction between the floating rotor motion and the surrounding flow. To address this shortcoming, additional simulations are performed by directly coupling the OpenFAST turbine with a simultaneous SOWFA large-eddy simulation of the surrounding wind flow. The two-way coupling between the OpenFAST turbine and the SOWFA flow field is achieved via an actuator line model and is updated every time step to capture the feedback between rotor motion and the surrounding fluid flow. This coupled SOWFA-OpenFAST model is described in more detail in the authors' previous work.<sup>25,29</sup>

The simulation workflow in this study follows three main stages, as illustrated in Figure 2. First, a “precursor” large-eddy simulation in SOWFA establishes the stably-capped neutral atmospheric boundary layer with no turbine present. This precursor simulation develops the turbulent structures and wind shear profile over 5.5 h, on a uniform 10-m cubic mesh in a domain with dimensions of 8 km by 2 km by 1 km and lateral periodic boundaries (see Figure 2). This precursor simulation provides the initial condition and boundary condition time histories for the next simulation stage. In the second stage, SOWFA simulations capture the flow surrounding the turbine for 70 min. These turbine-focused simulations are carried out in a smaller domain with dimensions 1.8 km by 1 km by 1 km, with inflow/outflow  $x$  boundaries and periodic  $y$  boundaries. These SOWFA simulations contain either an actuator line model with the coupled OpenFAST turbine (for the coupled inflow approach) or a sampling plane at the hypothetical rotor's undisplaced location (for the prerecorded inflow approach). In both situations, the uniform cubic 10-m mesh is refined to 1.25 m around the rotor, with a larger refinement region to 2.5 m in the turbine wake region. Figure 2 illustrates this domain, the mesh refinement regions, and the sampling plane location. The third stage consists of stand-alone OpenFAST simulations of the turbine over 70 min, using the prerecorded SOWFA inflow wind time series as described above. Similar precursor simulations and similar coupled SOWFA-OpenFAST simulations are described in further detail in the authors' previous work.<sup>25,26</sup>

## 2.4 | Case descriptions

To study how power generation is affected by floating platform displacements, a total of 36 simulations of an individual turbine is performed using the same inflow wind from SOWFA. The baseline case represents a fixed-bottom turbine, with all platform displacements set to a constant value of 0. All values for power generation by floating turbines are compared to this baseline case. To better understand how platform type

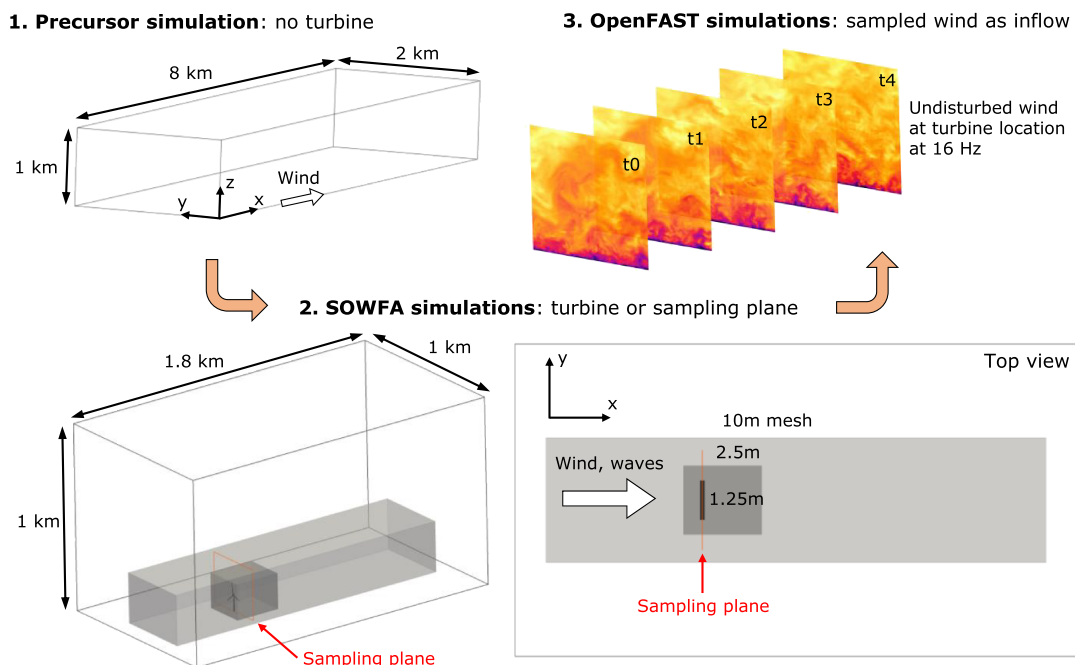


**FIGURE 2** Three-stage simulation workflow: (1) a “precursor” large-eddy simulation in SOWFA that develops the atmospheric boundary layer, (2) SOWFA large-eddy simulations that contain either a coupled OpenFAST turbine or a sampling plane at the rotor, and (3) stand-alone OpenFAST turbine simulations using the sampled SOWFA time series as inflow wind. The SOWFA simulation domain, mesh refinement regions, and sampling plane location are illustrated, including a top view

affects power generation and to identify underlying physical effects that can be generalized for any platform type, all cases with floating turbines are repeated for both the spar and semisubmersible platforms. The main floating case represents a typical floating turbine, with platform displacements in all 6 degrees of freedom (surge, sway, heave, pitch, roll, and yaw) causing rotor displacements in  $x_{rc}$ ,  $y_{rc}$ ,  $z_{rc}$ ,  $\phi_{rc}$ , and  $\theta_{rc}$ . These displacements generally consist of dynamic motion (“dynamic displacement”) around some time-averaged value (“time-averaged displacement”). The all-displacements floating case (for the spar and semisubmersible) and the fixed-bottom baseline case are performed using both the prerecorded inflow slices approach and the two-way coupled inflow approach. To limit computational cost, the remaining cases discussed next are performed using the prerecorded inflow approach only.

To better understand how individual platform degrees of freedom affect power generation, an additional set of cases restricts platform displacements to 1 or 2 degrees of freedom. For these cases, the nonactive degrees of freedom are set to a constant displacement of 0, with motion disabled in that direction. Each platform degree of freedom (surge, sway, heave, pitch, roll, and yaw) is simulated in isolation in this manner, as well as a case with both surge and pitch enabled together, for both platforms. Within this simulation framework, it is not possible to isolate individual rotor displacements directly, only platform displacements. Still, some of these cases can serve as proxies for isolating rotor displacements: For example, the surge-only case produces only  $x_{rc}$  displacements.

The floating cases described so far include both dynamic and time-averaged displacements. To better separate the effects of these two categories of displacement, another set of cases isolates the time-averaged displacement by disabling dynamic platform motions. For this set, each of the floating cases described above is repeated, but with the active degrees of freedom set to a constant displacement equal to the mean value from the previous cases. Conversely, the dynamic motion effect cannot be isolated in this simulation framework; this would require artificially prescribing displacement time histories with the time-averaged value subtracted out. However, the other floating cases that include both dynamic and time-averaged displacements still provide insight into the dynamic displacement effect.

### 3 | SIMULATION RESULTS

Each simulated case described in Section 2.4 produces 70-min time histories for power generation, platform displacements, and rotor displacements. The first 10 min of each time history are discarded to remove any transient startup effects, producing time histories of 60 min for analysis. In this section, the rotor and platform displacements that affect power generation are identified. The important rotor and platform displacements are then compared across platform type and across inflow approach. The difference in power generation between the floating cases and the fixed-bottom turbine is then linked to specific types of rotor displacements, explaining the underlying physical reasons for power losses or gains associated with floating wind turbines.

#### 3.1 | Negligible effect of crosswind and vertical displacements

For the simulated conditions with both wind and waves aligned with the  $x$  axis, power generation is unaffected by crosswind and vertical rotor displacements, specifically  $y_{rc}$ ,  $z_{rc}$ , and  $\theta_{rc}$ . The associated platform displacements in sway, heave, roll, and yaw are small for the simulated conditions and cause rotor displacements that are too small to significantly affect the average power. Comparing the case with all displacements enabled to the case with surge and pitch enabled, the average power agrees within 0.3%, indicating that the other displacements do not significantly affect the power. These unimportant displacements and results from cases that isolate the corresponding platform degrees of freedom are not discussed further, but are documented in Appendix A. Instead, the analysis focuses on displacements that do affect the power: the downwind rotor displacement  $x_{rc}$  and the rotor “pitch” angle  $\phi_{rc}$ , caused by platform surge and pitch.

#### 3.2 | Platform and rotor displacements

Understanding power generation in floating wind turbines requires understanding the underlying platform and rotor displacements that ultimately affect that power. The OpenFAST simulations record platform displacements, which are used to calculate rotor displacements based on simple geometry. For example, the downwind rotor displacement  $x_{rc}$  and rotor “pitch” angle  $\phi_{rc}$  are calculated from the platform surge and pitch, neglecting the small platform yaw displacement and tower bending effects:

$$\begin{aligned} x_{rc} &= \text{Surge} + z_H \sin(\text{Pitch}) \\ \phi_{rc} &= \text{Pitch}, \end{aligned} \quad (1)$$

where  $z_H$  is the distance between the platform origin and rotor center (90 m for the NREL 5-MW reference turbine<sup>21</sup>).

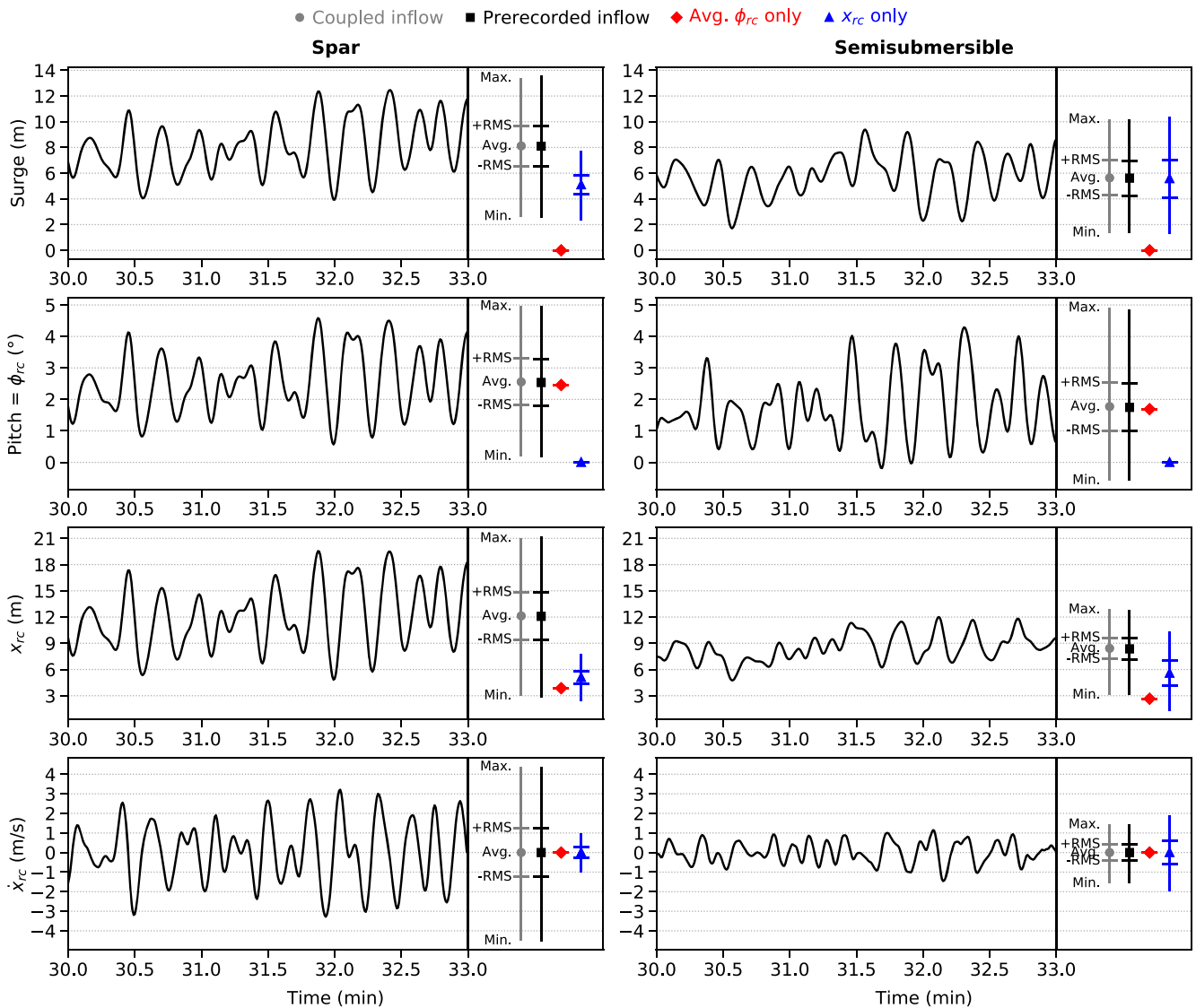


**FIGURE 3** Partial time histories of platform surge, rotor angle  $\phi_{rc}$ , rotor center location  $x_{rc}$ , and rotor center speed  $\dot{x}_{rc}$  from the prerecorded inflow case for spar (left) and semisubmersible (right) floating platforms. Key metrics of the entire time history, including the average, root-mean-square, minimum, and maximum values, are shown for four cases, including cases where the displacements are restricted to only the time-averaged  $\bar{\phi}_{rc}$  value or only  $x_{rc}$  displacements

Figure 3 presents partial time histories for the rotor and platform displacements that affect power: platform surge, rotor angle  $\phi_{rc}$  (equivalent to platform pitch), rotor center location downwind  $x_{rc}$ , and the resulting rotor center speed  $\dot{x}_{rc}$ . The time histories shown are for the case with prerecorded inflow and all displacements enabled. Additionally, the entire 60-min time histories are summarized using four metrics: the time-average, the root-mean-square (RMS), the minimum, and the maximum. Figure 3 includes summary metrics for four different cases: all displacements enabled with coupled inflow, all displacements enabled with prerecorded inflow, only average  $\bar{\phi}_{rc}$  (via platform pitch) displacement with prerecorded inflow, and only  $x_{rc}$  displacements (via platform surge) with prerecorded inflow.

As shown in Figure 3, the coupled inflow case (gray circle) has nearly identical platform and rotor displacements as the prerecorded inflow case (black square). For example, the average values for  $\phi_{rc}$  and  $x_{rc}$  agree within 1.5%, and the RMS values for  $\phi_{rc}$ ,  $x_{rc}$ , and  $\dot{x}_{rc}$  agree within 1%. This is expected, because both cases use OpenFAST to compute the platform displacements regardless of inflow approach. In contrast, the displacements in Figure 3 vary significantly between the other cases and between the spar and semisubmersible.

Differences between the spar and semisubmersible displacements in Figure 3 are largely caused by the platforms' different geometries and center of mass locations. The spar center of mass is 89.9 m below still water level,<sup>24</sup> but the semisubmersible center of mass is much higher at only 13.5 m below still water level.<sup>23</sup> In Figure 3, the rotor aerodynamic thrust causes the nonzero averages for  $\phi_{rc}$  and  $x_{rc}$ , as also observed by Liu et al.<sup>4</sup> However, the spar average  $\bar{\phi}_{rc} = 2.5^\circ$  is 45% larger than the semisubmersible average  $\bar{\phi}_{rc} = 1.7^\circ$ .

In Figure 3, the two platforms have similar RMS values for  $\phi_{rc}$ , but the spar RMS values for  $x_{rc}$  and  $\dot{x}_{rc}$  are 1.5 m (125%) larger and 0.8 m/s (197%) larger for the semisubmersible. This is partially because the lower center of mass for the spar creates a longer rotation arm to the rotor center, compared to the semisubmersible. So, similarly sized RMS platform pitch values are amplified into larger RMS  $x_{rc}$  values for the spar than for the semisubmersible. In fact, platform pitch rotation is the dominant driver of  $x_{rc}$  displacements for the spar, but not for the semisubmersible: The spar has a 99% correlation between the pitch and  $x_{rc}$  time histories, but the semisubmersible only has a 36% correlation. These different correlation levels between  $x_{rc}$  and pitch (or  $\phi_{rc}$ ) are also evident in the time histories in Figure 3.

The center of mass location also helps explain correlation patterns between platform surge and pitch. The spar platform surge is strongly positively correlated to platform pitch at a +97% correlation coefficient, so that large positive pitch variations occur at the same time as positive surge variations (see Figure 3). In contrast, the semisubmersible platform surge is somewhat negatively correlated to platform pitch at a -56% correlation coefficient, so that large positive pitch variations occur at the same time as negative surge variations (see Figure 3). This is partially because OpenFAST reports platform displacements with respect to a platform origin at still water level,<sup>30</sup> rather than the center of rotation. Therefore, the reported platform surge is partly caused by platform rotation, rather than a purely linear displacement of the center of rotation. Figure 4 illustrates the scenario where platform pitch rotation, about the center of rotation, causes a reported platform surge and  $x_{rc}$  rotor displacement. The spar center of rotation is far below still water level, so that positive pitch angles significantly increase the reported platform surge at still water level. In contrast, the semisubmersible center of rotation is much closer to still water level because of its high center of mass, so that positive pitch angles do not affect the reported platform surge as much.

The influence of platform pitch on both  $x_{rc}$  and reported platform surge also explains why the surge-only case has different  $x_{rc}$  displacements than the cases with all displacements enabled. In Figure 3, the  $x_{rc}$ -only case (blue triangle) is simulated by enabling surge platform displacements only and is therefore missing the contribution of platform pitch to reported surge and  $x_{rc}$ . So, the  $x_{rc}$  and  $\dot{x}_{rc}$  RMS values are significantly different between this case and the other cases: The spar has  $x_{rc}$  and  $\dot{x}_{rc}$  RMS values that are 2.0 m (72%) and 1.0 m/s (77%) smaller for this case, whereas the semisubmersible values are 0.2 m (20%) and 0.2 m/s (41%) larger for this case.

Finally, both surge and pitch must be enabled concurrently to obtain realistic rotor displacements, because isolating surge or pitch changes their displacement metrics and  $x_{rc}$  results from both surge and pitch. Still, power is directly affected by rotor displacements, so power effects are best explained by focusing on rotor displacements  $x_{rc}$  and  $\phi_{rc}$ , with the awareness that  $x_{rc}$  displacements are caused by a combination of platform surge and pitch.

### 3.3 | Power generation

The turbine displacements summarized in Figure 3 affect the power generation of the floating wind turbine. Figure 5 presents the difference in power between floating turbine cases and an equivalent fixed-bottom turbine baseline case, where the solid bars represent the simulation results.

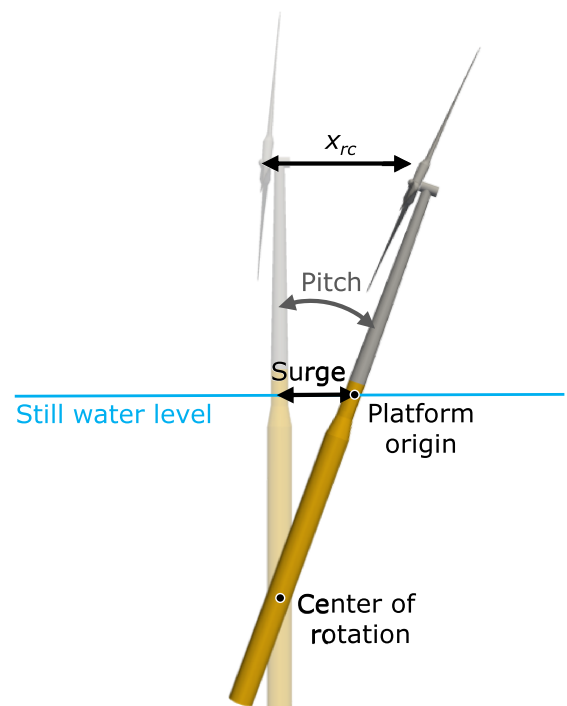


**FIGURE 4** Side view of a scenario where pitch rotation, about the center of rotation, creates a reported platform surge because of the distance from the center of rotation to the platform origin, where surge is reported. Similarly, this pure platform rotation creates a linear displacement  $x_{rc}$  at the rotor center

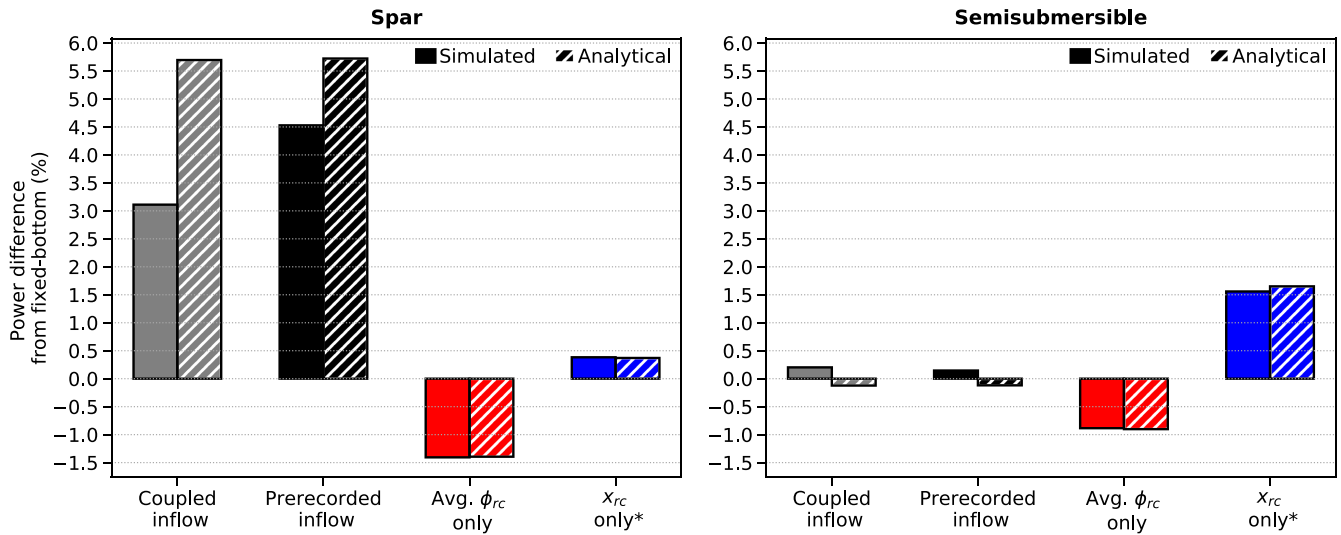


**FIGURE 5** Percent difference in power generation, relative to an equivalent fixed-bottom turbine, of spar (left) and semisubmersible (right) floating wind turbines. Simulated power gains/losses (solid bars) are compared to predictions from the analytical model (striped bars) for four cases. \*The  $x_{rc}$  only case has different rotor displacements than the other cases, see Figure 3

The striped bars represent results from the proposed analytical model and are discussed in Section 4. These power differences are compared across four different cases: all displacements enabled with coupled inflow, all displacements enabled with prerecorded inflow, only average  $\bar{\phi}_{rc}$  displacement with prerecorded inflow, and only  $x_{rc}$  displacements with prerecorded inflow.

Figure 5 illustrates that coupled inflow (gray) and prerecorded inflow (black) generate slightly different amounts of power, despite agreeing well on rotor displacements (see Figure 3). Specifically, the prerecorded inflow approach predicts lower power generation than the coupled inflow approach for all three platform types: The prerecorded cases' power predictions are 2.0%, 3.4%, and 3.3% smaller than the coupled cases' for the spar, semisubmersible, and fixed-bottom platforms, respectively. This power difference is caused by the two inflow methods' models for rotor-flow interactions. Although both inflow approaches rely on an actuator line model, the prerecorded inflow method uses AeroDyn's dynamic blade element momentum theory model to estimate rotor wake and induction effects.<sup>19</sup> In contrast, the coupled inflow approach directly captures these effects by allowing the blade node forces to affect the surrounding flow.<sup>29</sup>

### 3.3.1 | Time-averaged displacement effect on power

To examine how average rotor angle  $\bar{\phi}_{rc}$  affects the average power, compare the prerecorded inflow case with all displacements enabled to the case with only average  $\bar{\phi}_{rc}$  in Figure 5. The nonzero average  $\bar{\phi}_{rc}$  causes a 0.9%–1.4% power loss compared to the fixed-bottom case, because it increases the angle of the relative wind and therefore reduces aerodynamic performance. In contrast, the nonzero average  $x_{rc}$  displacement does not affect the power, because statically shifting the rotor downwind does not affect its aerodynamic performance: The case with only average  $x_{rc}$  displacement (not pictured) produces the same power as the fixed-bottom case (see Appendix A). Comparing between the two platforms, the spar power loss is 1.6 times the semisubmersible power loss for the average- $\bar{\phi}_{rc}$ -only case, because the spar average  $\bar{\phi}_{rc}$  angle is 1.4 times the semisubmersible average  $\bar{\phi}_{rc}$  (see Figure 3).

### 3.3.2 | Dynamic displacement effect on power

In general, dynamic displacements in  $x_{rc}$  create power gains compared to the fixed-bottom case, because it adds a relative rotor velocity  $\dot{x}_{rc}$  to the inflow wind speed. Though  $\dot{x}_{rc}$  can take both positive and negative values, the additional motion causes a net power gain when averaged over time. Although dynamic displacements cannot be simulated separately from time-averaged displacements in this simulation framework, the case with only  $x_{rc}$  displacements (both average and dynamic) does offer evidence that dynamic  $x_{rc}$  displacements cause power gains. Average  $x_{rc}$  does not affect the power, implying that the entire 0.4%–1.6% power gain for the  $x_{rc}$  case (see Figure 5) is caused by the dynamic  $x_{rc}$  displacements. Comparing between the two platforms, the semisubmersible power gain caused by dynamic  $x_{rc}$  is 4.1 times the spar power gain (see Figure 5), because the  $x_{rc}$  and  $\dot{x}_{rc}$  variations are larger for the semisubmersible, as measured by the RMS values (see Figure 3).

### 3.3.3 | Total floating effect on power: Dynamic and time-averaged displacements

The total effect of floating platforms on power is a balance between the time-averaged and dynamic displacement effects, specifically a balance between the power loss due to average  $\bar{\phi}_{rc}$  and the power gain due to dynamic  $x_{rc}$  displacements. This balance explains why the all-displacement case results in a large 4.1%–4.5% power gain for the spar, but a negligible 0.1%–0.2% power gain for the semisubmersible (see Figure 5): The spar  $\dot{x}_{rc}$  variations are 197% larger than for the semisubmersible, which outweighs the 45% larger average  $\bar{\phi}_{rc}$  to create a substantially larger power gain.

In Figure 5, it appears that the power gains in the all-displacement cases are not a simple superposition of the average  $\bar{\phi}_{rc}$ -only power loss and the  $x_{rc}$ -only power gain. However, the  $x_{rc}$ -only case has substantially different  $x_{rc}$  displacements than the all-displacement cases, as discussed in Section 3.2, so power gains should not be directly compared between the  $x_{rc}$ -only case and the all-displacement cases.

Finally, these power results are all based on a below-rated wind speed of 8 m/s. When the turbine is operating at above-rated wind speeds in control region 3, power loss caused by average  $\bar{\phi}_{rc}$  may be insignificant, because the turbine is capped at rated power regardless. For above-rated wind speeds, the size of any power gain caused by dynamic  $x_{rc}$  displacements likely depends on how the blade pitch controller interacts with the displacement frequencies. However, the trends in platform displacements, rotor displacements, and power generation discussed in this section generally hold true for nonaligned wind and waves, as indicated by similar simulations with 30° misalignment between the wind and wave directions conducted by the authors. The simulated results are also generally consistent with limited field measurements from the Hywind Demo and WindFloat WF1 projects, as reported in Roddier et al.<sup>31</sup> In particular, the WF1 semisubmersible generated power on par with an equivalent fixed-bottom turbine.<sup>31</sup> Also, the Hywind Demo spar required introducing a platform control system for above-rated wind speeds to reduce unacceptably large platform pitch displacements, although how this affected power generation is not documented.<sup>31</sup>

## 4 | ANALYTICAL MODELS FOR POWER GENERATION

Based on the simulation results in Section 3, simple analytical models are proposed for estimating the power generation from floating wind turbines in the below-rated operating region. As discussed in Section 3, the total floating effect on power generation is a combination of the effects of average  $\bar{\phi}_{rc}$  displacement and dynamic  $x_{rc}$  displacement (caused by surge and pitch). The final proposed analytical model is a combination of two analytical submodels for each of these effects.

The proposed analytical models predict the difference between a floating wind turbine and an equivalent fixed-bottom turbine using basic momentum theory. First, a review of the derivation for a fixed-bottom turbine's power is presented. A turbine's power  $P$  depends on its power coefficient  $C_p$  and the power available in the wind  $P_{wind}$ , given by the kinetic energy flux of the wind  $\vec{U}$  through the rotor disc area  $\vec{A}$ :

$$\begin{aligned} P &= C_p P_{wind} \\ &= C_p \int_A \frac{1}{2} |\vec{U}|^2 (\rho \vec{U} \cdot d\vec{A}) \\ &= C_p \frac{1}{2} \rho |\vec{U}|^2 \vec{U} \cdot \vec{A}, \text{ if } \vec{U} \text{ is uniform over } \vec{A}. \end{aligned} \quad (2)$$

The power  $P_{fb}$  produced by a fixed-bottom turbine with no rotor displacement, in a uniform wind field of  $\vec{U} = U\hat{i}$ , is then the well-known

$$P_{fb} = \frac{1}{2} \rho C_p A U^3. \quad (3)$$

If the rotor is moving or angled with respect to the wind, Equation (2) can be adapted by considering the reference frame of the turbine, where the rotor area  $\vec{A}$  remains unchanged but the wind vector  $\vec{U}$  becomes the relative wind vector  $\vec{U}_{rel}$ . The instantaneous power coefficient  $C_p$  is also altered due to modified aerodynamic performance, but the simple analytical models presented here assume that  $C_p$  is constant over time and also consistent between floating and fixed turbines.

### 4.1 | Average $\phi_{rc}$ displacement model

The first model considers a rotor at an angle  $\phi$  relative to a uniform wind field with wind speed  $U$ . In the reference frame of the rotor, the relative wind vector is  $\vec{U}_{rel} = U \cos \phi \hat{i}$  and the rotor area is  $\vec{A} = A \hat{i}$ . Assuming a constant power coefficient  $C_p$  in Equation (2), the angled turbine's power is

$$P(\phi) = \frac{1}{2} \rho C_p \int_A (U \cos \phi)^3 dA = P_{fb} \cos^3 \phi. \quad (4)$$

If the angle  $\phi$  is static over time, then Equation (4) directly gives the time-averaged power, assuming  $U$  is steady. This variety of  $\cos^n \cos^n \varphi$  model is commonly used for angled rotors (especially rotors at a constant yaw) throughout the literature,<sup>15,32</sup> with  $n = 3$  as a common exponent.<sup>15</sup> Different experiments suggest values of  $n$  varying from 1 to 5 for yawed rotors.<sup>15,33</sup>

On the other hand, if  $\phi$  varies in time, the entire  $P_{fb} \cos^3 \varphi$  term should be averaged to get the time-averaged  $\bar{P}(\phi)$ . Despite this, the proposed average pitch model assumes that the effect of a dynamically varying rotor angle  $\phi(t)$  can be approximated by a constant rotor angle at the time-averaged value  $\bar{\phi}$ :

$$\bar{P}(\phi) = \bar{P}_{fb} \cos^3 \bar{\phi}. \quad (5)$$

Equation (5) can be used to model how average rotor “pitch”  $\bar{\phi}_{rc}$  changes power generation in floating wind turbines. In this case, the overall angle  $\bar{\phi}$  between the wind vector and the rotor disk should incorporate both the platform-induced angle  $\phi_{rc}$  and the shaft tilt angle  $\phi_t$  ( $5^\circ$  for the NREL 5-MW reference turbine<sup>21</sup>). The shaft tilt angle is typically ignored in yawed rotor analysis or implicitly included in  $P_{fb}$ . However, for a rotor with an average angle caused by platform pitch, the power is better modeled by explicitly including the shaft tilt angle as a constant rotor angle, for both the floating turbine and the fixed-bottom turbine. In this situation, Equation (5) becomes

$$\bar{P}_{fb} = \bar{P}(\phi = 0) \cos^3 \phi_t \quad (6)$$

for the fixed-bottom turbine and

$$\begin{aligned} \bar{P}(\bar{\phi}_{rc} + \phi_t) &= \bar{P}(\phi = 0) \cos^3(\bar{\phi}_{rc} + \phi_t) \\ &= \bar{P}_{fb} \cos^3(\bar{\phi}_{rc} + \phi_t) / \cos^3 \phi_t \end{aligned} \quad (7)$$

for the turbine with an average pitch displacement. The shaft tilt angle can similarly be incorporated into a yawed rotor model. Note that this model predicts that a positive  $\phi_{rc}$  always works to decrease the average power generation, which is consistent with the simulated results. Equation (7) is the proposed analytical model for describing the effect of average rotor angle  $\phi_{rc}$  on power generation.

## 4.2 | Dynamic $x_{rc}$ displacement model

The second model considers a rotor perpendicular to the steady wind vector  $\vec{U} = U\hat{i}$ , moving forward and backward into the wind with motion  $x_{rc}(t)$ . The relative wind vector is  $\vec{U}_{rel} = (U + \dot{x}_{rc})\hat{i}$  and the rotor area is  $\vec{A} = A\hat{i}$ . Assuming a constant power coefficient  $C_p$  in Equation (2), the moving turbine's power is

$$P(t) = \frac{1}{2} \rho C_p \int_A (U + \dot{x}_{rc})^3 dA = \frac{1}{2} \rho C_p A (U + \dot{x}_{rc})^3, \text{ if } U \text{ is uniform over } A. \quad (8)$$

To further simplify the model, let the rotor velocity  $\dot{x}_{rc}$  be modeled as a sine curve with angular frequency  $\omega$  and amplitude  $V_{rc}$ , such that  $\dot{x}_{rc} = V_{rc} \sin(\omega t)$ . The time-averaged power is then obtained by integrating over one period:

$$\bar{P} = \frac{\omega}{2\pi} \frac{1}{2} \rho C_p A \int_{-\pi/\omega}^{\pi/\omega} (U + \dot{x}_{rc})^3 dt = \frac{\omega}{2\pi} \frac{1}{2} \rho C_p A \int_{-\pi/\omega}^{\pi/\omega} (U + V_{rc} \sin(\omega t))^3 dt = \frac{1}{2} \rho C_p A U^3 \left( 1 + \frac{3V_{rc}^2}{2U^2} \right) = \bar{P}_{fb} \left( 1 + \frac{3V_{rc}^2}{2U^2} \right), \quad (9)$$

since the odd-powered sine terms in the cubic expansion integrate to 0. Note that this model predicts that  $x_{rc}$  motions always work to increase time-averaged power, which is consistent with the simulated results. The model given by Equation (9) is similar to analytical models proposed by Wen et al. for sinusoidal platform surge and sinusoidal pitch.<sup>11,12</sup> However, the models by Wen et al. separate surge from pitch, rather than

considering the rotor center velocity  $\dot{x}_{rc}$  caused by both surge and pitch together. Wen et al.'s pitch model also explicitly assumes  $\phi_{rc}$  is small enough that  $\cos(\phi_{rc}) \approx 1$ , which neglects the average pitch effect modeled by Equation (7).

Equation (9) can be used to model how dynamic  $x_{rc}$  displacements affect power generation for floating platforms. Numerical differentiation of  $x_{rc}(t)$  produces a time history for the rotor center  $x$  velocity  $\dot{x}_{rc}(t)$ , which can be approximated by a sine curve with amplitude  $V_{rc}$ , as in Equation (9). For these simulations, the  $\dot{x}_{rc}(t)$  time history does not directly fit a sine curve well (see Figure 3). So a proxy  $V_{rc}$  amplitude is computed from the RMS of the  $\dot{x}_{rc}(t)$  time history using  $V_{rc} = \sqrt{2} \text{RMS}(\dot{x}_{rc})$ , where the factor of  $\sqrt{2}$  is determined by the ratio of amplitude to RMS for all sine curves. Equation (9) with the RMS approximation for  $V_{rc}$  is the proposed analytical model for describing the effect of dynamic  $x_{rc}$  displacements on power generation.

### 4.3 | Total floating model: Dynamic and time-averaged displacements

The final model considers a floating wind turbine's rotor that is free to move under the influence of all six platform degrees of freedom. As discussed in Section 3, the power generation of this rotor is predominantly affected by both the time-averaged rotor angle  $\bar{\phi}_{rc}$  and dynamic  $x_{rc}$  displacements, caused by platform surge and pitch. To model the overall power difference between this floating turbine and an equivalent fixed-bottom turbine, the analytical model for average  $\bar{\phi}_{rc}$  displacement (Section 4.1) is combined with the analytical model for dynamic  $x_{rc}$  displacements (Section 4.2).

Specifically, this total floating model treats the rotor as translating horizontally according to  $x_{rc}$  while also angled at a constant value given by the time-averaged  $\phi_{rc}$  (plus shaft tilt). In the reference frame of the rotor, the relative wind vector is then

$$\vec{U}_{rel} = (U + \dot{x}_{rc}) \cos(\bar{\phi}_{rc} + \phi_t) \hat{i} \quad (10)$$

and the rotor area is  $\vec{A} = A \hat{i}$ . Note that the  $\cos(\bar{\phi}_{rc} + \phi_t) \hat{i}$  term in Equation (10) does not vary in time, so it can be moved outside the time integral when calculating the time-averaged power generation. Following similar steps as in Sections 4.1 and 4.2, the time-averaged power generated by this floating wind turbine is

$$\bar{P} = \bar{P}_{fb} \left( 1 + \frac{3V_{rc}^2}{2U^2} \right) \cos^3(\bar{\phi}_{rc} + \phi_t) / \cos^3 \phi_t, \quad (11)$$

assuming a constant  $C_p$ , an average rotor angle of  $\bar{\phi}_{rc}$ , a shaft tilt of  $\phi_t$ , and a sine curve model for the rotor center velocity:  $\dot{x}_{rc} = V_{rc} \sin(\omega t)$ .

Equation (11) is the proposed model for how a floating wind turbine's power generation compares to a fixed-bottom turbine's power overall, including effects from both average rotor angle as well as dynamic  $x_{rc}$  displacements. For no rotor motion ( $V_{rc} = 0$ ), this total floating model reduces to the average rotor angle model in Equation (7). For no average rotor angle ( $\bar{\phi}_{rc} = 0$ ), this total floating model reduces to the dynamic  $x_{rc}$  displacement model in Equation (9).

### 4.4 | Analytical model performance

Figure 5 compares power gain predictions from the total-floating-effect analytical model in Equation (11) (striped bars) to the simulated power results discussed in Section 3 (solid bars), for both the spar and semisubmersible. The analytical model agrees with the simulations that the all-displacement spar cases show a significant power gain, although the semisubmersible only shows a small power difference (see Figure 5). However, this basic analytical model does not perfectly agree with the magnitude of the simulated power gains/losses.

For the case with only average  $\bar{\phi}_{rc}$ , the analytical model performs well, with a ratio of 0.99–1.02 between the analytical and simulated power losses (see Figure 5). This indicates that the analytical model can reasonably predict how a constant  $\phi_{rc}$  angle affects power generation. For the case with only  $x_{rc}$  displacements, the analytical model also performs well, with a ratio of 0.96–1.06 between the analytical and simulated power losses (see Figure 5). This indicates that the dynamic displacement model with the RMS approximation for  $\dot{x}_{rc}$  amplitude reasonably captures the simulated power gain due to dynamic  $x_{rc}$  displacements.

However, for the all-displacement cases which are more representative of a real turbine, the analytical model does not perfectly predict the power gain/loss magnitude, with ratios of 0.81–1.83 between the analytical and simulated power gains/losses (see Figure 5). This disagreement in power gain/loss magnitude indicates that the analytical model does not fully capture some simulated effect. Several adjustments to the model were attempted to address this disagreement:

- *Removing the sine approximation for  $\dot{x}_{rc}$* : the simulated time history for  $\dot{x}_{rc}$  was used in Equation (10) instead of using the sine curve approximation, and then this time history was averaged over time to replace the  $3V_{rc}^2/2U^2$  term in Equation (11).
- *Removing the constant-angle approximation for the average pitch effect*: as well as using the time history for  $\dot{x}_{rc}$ , the simulated  $\phi_{rc}$  time history replaced the time-averaged angle  $\bar{\phi}_{rc}$  in Equation (10) and then the entire term  $(U + \dot{x}_{rc})\cos(\phi_{rc} + \phi_t)$  was averaged over time.
- *Removing the steady wind approximation*: the simulated time history for  $U$  at hub height was used instead of assuming steady wind, and then the entire term  $(U + \dot{x}_{rc})\cos(\phi_{rc} + \phi_t)$  was again averaged over time using simulated time histories for  $U$ ,  $\dot{x}_{rc}$ , and  $\phi_{rc}$ .

However, these attempted adjustments did not clearly improve the model performance for power gain/loss magnitude. Possible reasons for the continued disagreement include assuming that  $C_p$  is constant, although  $C_p$  actually varies in time as the relative inflow wind fluctuates. This effect is difficult to capture with a model of comparable simplicity, but one possibility is to adjust the instantaneous  $C_p$  using an empirical relationship between  $C_p$  and tip speed ratio (possibly filtered and with a time delay to account for the variable-speed controller). The disagreement may also be partially caused by only including the effect of instantaneous rotor angle  $\phi_{rc}$  at the rotor center, rather than across the height of the rotor disc. This could explain why the analytical model performs better for the  $x_{rc}$ -only case, where platform pitch does not contribute the  $x_{rc}$  displacements.

## 5 | CONCLUSIONS

OpenFAST simulations of the NREL 5-MW reference turbine are performed for three platform types: the OC3-UMaine spar, the OC4-DeepCWind semisubmersible, and a fixed-bottom counterpart with no platform displacements. These simulations examine how platform and rotor displacements, both dynamic and time-averaged, affect the average power generation of floating wind turbines for a single combination of a below-rated wind speed and extreme wave height. The main conclusions of this study are the following:

- Overall power gains or losses in floating wind turbines are primarily caused by a balance between two competing effects:
  - Power decreases caused by average rotor pitch angle ( $\bar{\phi}_{rc}$ ) driven by platform pitch, and
  - Power increases caused by dynamic rotor motions upwind-downwind ( $x_{rc}$ ) driven by platform surge and pitch motions, which change the relative wind velocity at the rotor.
- Rotor displacements caused by platform sway, heave, roll, and yaw do not significantly affect the average power.
- Contrary to the common practice of isolating platform surge or pitch when studying floating platforms, surge, and pitch must be enabled concurrently to accurately capture the power generated by floating wind turbines, for two reasons:
  - Isolating surge or pitch changes displacement characteristics and
  - Both surge and pitch contribute to the dynamic rotor motions upwind-downwind ( $x_{rc}$ ).
- The spar's lower center of mass creates larger, pitch-dominated rotor motions upwind-downwind, which outweigh its larger average rotor pitch angle to cause a 3.1%–4.5% power gain compared to a fixed-bottom wind turbine.
- The semisubmersible has smaller rotor motions upwind-downwind, which barely outweigh the smaller average rotor pitch angle to cause an insignificant (0.1%–0.2%) power gain.
- The simple analytical model proposed in Equation (11) reasonably predicts power differences caused by floating platforms, but the magnitude of the predicted gain/loss can be improved.

In summary, although predicting floating-turbine power is vital for floating wind farm design and economics, this study indicates that floating platforms do not provide universally significant power gains compared to fixed-bottom wind turbines; a closer analysis of details in the platform's displacement behavior is required for such a prediction. Future research in this area should examine additional environmental conditions, especially near-rated wind speeds and lower wave heights. The trends observed here should be confirmed by field measurements, when available. Field measurements, experiments, and additional simulations with simplified environmental conditions could also inform significant improvements to the proposed analytical model, with a focus on a time-varying power coefficient and instantaneous pitch angle effects.

## ACKNOWLEDGEMENTS

The authors thank Jason Jonkman and Amy Robertson of NREL for their advice during the preliminary stages of this work. This study is supported by a Graduate Research Fellowship from the National Science Foundation, grant #1451512. This work used the Extreme Science and Engineering

Discovery Environment (XSEDE), which is supported by National Science Foundation grant #ACI-1548562. This work also used NREL computational resources sponsored by the U.S. Department of Energy Office of Energy Efficiency and Renewable Energy.

## DISCLAIMER

This work was authored (in part) by NREL, operated by Alliance for Sustainable Energy, LLC, for the U.S. Department of Energy (DOE) under contract DE-AC36-08GO28308. Funding for NREL is provided by the DOE Office of Energy Efficiency and Renewable Energy, Wind Energy Technologies Office. The views expressed in the article do not necessarily represent the views of the DOE or the U.S. Government. The U.S. Government retains (and the publisher, by accepting the article for publication, acknowledges that the U.S. Government retains) a non-exclusive, paid-up, irrevocable, worldwide license to publish or reproduce the published form of this work, or allow others to do so, for U.S. Government purposes.

## PEER REVIEW

The peer review history for this article is available at <https://publons.com/publon/10.1002/we.2608>.

## REFERENCES

- Musial W, Beiter P, Spitsen P, Nunemaker J, Gevorgian V. 2018 Offshore wind technologies market report. Tech. Rep. DOE/GO-102019-5192, U.S. Department of Energy; 2018.
- Veers P, Dykes K, Lantz E, et al. Grand challenges in the science of wind energy. *Science*. 2019;366(6464):eaau2027.
- Thiagarajan KP, Dagher HJ. A review of floating platform concepts for offshore wind energy generation. *J Offshore Mech Arct Eng*. 2014;136(2):20903.
- Liu Y, Xiao Q, Incecik A, Peyrard C, Wan D. Establishing a fully coupled CFD analysis tool for floating offshore wind turbines. *Renew Energy*. 2017;112:280-301.
- Tran TT, Kim D-H. A CFD study of coupled aerodynamic-hydrodynamic loads on a semisubmersible floating offshore wind turbine. *Wind Energy*. 2017;21:70-85.
- Huang Y, Wan D. Investigation of interference effects between wind turbine and spar-type floating platform under combined wind-wave excitation. *Sustainability*. 2020;12:246.
- Karimian Aliabadi S, Rasekh S. Effect of platform disturbance on the performance of offshore wind turbine under pitch control. *Wind Energy*. 2020;23(5):1210-1230.
- Lin L, Wang K, Vassalos D. Detecting wake performance of floating offshore wind turbine. *Ocean Eng*. 2018;156:263-276.
- Sant T, Bonnici D, Farrugia R, Micallef D. Measurements and modelling of the power performance of a model floating wind turbine under controlled conditions. *Wind Energy*. 2015;18:811-834.
- Shen X, Hu P, Chen J, Zhu X, Du Z. The unsteady aerodynamics of floating wind turbine under platform pitch motion. *Proc IMechE Part A: J Power Energy*. 2018;232(8):1019-1036.
- Wen B, Tian X, Dong X, Peng Z, Zhang W. Influences of surge motion on the power and thrust characteristics of an offshore floating wind turbine. *Energy*. 2017;141:2054-2068.
- Wen B, Dong X, Tian X, Peng Z, Zhang W, Wei K. The power performance of an offshore floating wind turbine in platform pitching motion. *Energy*. 2018;154:508-521.
- Wen B, Tian X, Dong X, Peng Z, Zhang W. On the power coefficient overshoot of an offshore floating wind turbine in surge oscillations. *Wind Energy*. 2018;21:1076-1091.
- Fleming P, Gebraad PMO, Lee S, et al. Simulation comparison of wake mitigation control strategies for a two-turbine case. *Wind Energy*. 2015;18(12):2135-2143.
- Micallef D, Sant T. A review of wind turbine yaw aerodynamics. In: Aissaoui AG, Tahour A, eds. *Wind turbines—Design, control and applications*. London: IntechOpen; 2016:27-53. <https://doi.org/10.5772/63445>
- Sebastian T, Lackner MA. Characterization of the unsteady aerodynamics of offshore floating wind turbines. *Wind Energy*. 2013;16:339-352.
- Wang J, Wang C, Castañeda OD, Campagnolo F, Bottasso CL. Large-eddy simulation of scaled floating wind turbines in a boundary layer wind tunnel. *J Phys Conf Ser*. 2018;1037:72032.
- Wen B, Tian X, Zhang Q, et al. Wind shear effect induced by the platform pitch motion of a spar-type floating wind turbine. *Renew Energy*. 2019;135:1186-1199.
- OpenFAST documentation (release v2.3.0). <https://openfast.readthedocs.io>. Accessed August 14, 2020; 2020.
- Churchfield M, Lee S. SOWFA: *Simulator for Wind Farm Applications*: National Renewable Energy Laboratory; 2020. <https://www.nrel.gov/wind/nwtc/sowfa.html>. Accessed December 28, 2020.
- Jonkman J, Butterfield S, Musial W, Scott G. Definition of a 5-MW reference wind turbine for offshore system development. Tech. Rep. NREL/TP-500-38060, National Renewable Energy Laboratory, Golden, Colorado; 2009.
- Robertson AN, Jonkman JM. Loads analysis of several offshore floating wind turbine concepts. In: Proceedings of ISOPE 2011, 21st International Offshore and Polar Engineering Conference. International Society of Offshore and Polar Engineers; 2011; Maui, Hawaii. ISOPE-1-11-204.
- Robertson A, Jonkman J, Masciola M, et al. Definition of the semisubmersible floating system for phase II of OC4. Tech. Rep. NREL/TP-5000-60601, National Renewable Energy Laboratory, Golden, Colorado; 2014.
- Jonkman J. Definition of the floating system for phase IV of OC3. Tech. Rep. NREL/TP-500-47535, National Renewable Energy Laboratory, Golden, Colorado; 2010.
- Johlas HM, Martínez-Tossas LA, Schmidt DP, Lackner MA, Churchfield MJ. Large eddy simulations of floating offshore wind turbine wakes with coupled platform motion. *J Phys Conf Ser*. 2019;1256:12018.

26. Johlas HM, Martínez-Tossas LA, Lackner MA, Schmidt DP, Churchfield MJ. Large eddy simulations of offshore wind turbine wakes for two floating platform types. *J Phys Conf Ser.* 2020;1452:12034.
27. Bachynski EE, Kvittem MI, Luan C, Moan T. Wind-wave misalignment effects on floating wind turbines: Motions and tower load effects. *J Offshore Mech Arct Eng.* 2014;136(4):41902.
28. Lee S, Churchfield M, Driscoll F, et al. Load estimation of offshore wind turbines. *Energies.* 2018;11(7):1895.
29. Churchfield MJ, Lee S, Michalakes J, Moriarty PJ. A numerical study of the effects of atmospheric and wake turbulence on wind turbine dynamics. *J Turbul.* 2012;13(14):1-32.
30. Jonkman JM, Buhl MLJ. FAST user's guide. Tech. Rep. NREL/TP-500-38230, National Renewable Energy Laboratory, Golden, Colorado; 2005.
31. Roddier D, Cermelli C, Weinstein J, et al. State-of-the-art. In: Cruz J, Atcheson M, eds. *Floating offshore wind energy.* Cham, Switzerland: Springer; 2016:271-331. [https://doi.org/10.1007/978-3-319-29398-1\\_6](https://doi.org/10.1007/978-3-319-29398-1_6)
32. Fleming P, Annoni J, Shah JJ, et al. Field test of wake steering at an offshore wind farm. *Wind Energy Sci.* 2017;2(1):229-239.
33. Schepers JG. Engineering models in wind energy aerodynamics: Development, implementation and analysis using dedicated aerodynamic measurements. *Ph.D. Thesis:* Delft University of Technology; 2012.

**How to cite this article:** Johlas HM, Martínez-Tossas LA, Churchfield MJ, Lackner MA, Schmidt DP. Floating platform effects on power generation in spar and semisubmersible wind turbines. *Wind Energy.* 2021;24:901-916. <https://doi.org/10.1002/we.2608>

**APPENDIX A: SIMULATION DATA**

The tables below give average, RMS, minimum, and maximum values for rotor center displacements and platform displacements from simulations with different platform degrees of freedom (DOFs) enabled. The time-averaged power for simulations with both dynamic and average displacements and with average displacements only is also presented. Tables A1 and A2 show data for the spar and semisubmersible platforms, respectively.

**TABLE A1** Spar data for time-averaged power for cases with the total floating displacements and average displacements only, as well as average, root-mean-square, minimum, and maximum values for rotor and platform displacements

Active DOF		All DOF, coupled inflow	All DOF	Surge and pitch	Surge	Sway	Heave	Roll	Pitch	Yaw
Power (MW) <sup>a</sup>	Total disp.	1.712	1.678	1.679	1.611	1.606	1.606	1.606	1.599	1.606
	Avg. disp.	-	1.582	1.583	1.606	1.606	1.606	1.606	1.583	1.606
$x_{rc}$ (m)	Avg.	12.129	12.080	12.062	5.092	-	-	-	1.717	-
	RMS	2.707	2.736	2.713	0.755	-	-	-	0.412	-
	Min.	3.010	2.853	2.911	2.335	-	-	-	0.355	-
	Max.	21.006	21.217	21.063	7.740	-	-	-	3.387	-
$y_{rc}$ (m)	Avg.	-0.309	-0.263	-	-	-0.009	-	-0.109	-	-
	RMS	0.078	0.091	-	-	0.045	-	0.069	-	-
	Min.	-0.531	-0.547	-	-	-0.130	-	-0.280	-	-
	Max.	-0.080	-0.011	-	-	0.118	-	0.051	-	-
$z_{rc}$ (m)	Avg.	-0.277	-0.273	-0.096	-	-	-0.072	-	-0.017	-
	RMS	0.292	0.288	0.053	-	-	0.307	-	0.008	-
	Min.	-1.201	-1.184	-0.329	-	-	-1.065	-	-0.064	-
	Max.	0.714	0.709	-	-	-	0.916	-	-0.001	-
$\phi_{rc}$ = Pitch (°)	Avg.	2.555	2.538	2.537	-	-	-	-	1.093	-
	RMS	0.743	0.750	0.743	-	-	-	-	0.262	-
	Min.	0.199	0.148	0.150	-	-	-	-	0.226	-
	Max.	4.962	4.961	4.904	-	-	-	-	2.157	-
$\theta_{rc}$ = Yaw (°)	Avg.	0.014	0.013	-	-	-	-	-	-	-0.006
	RMS	0.183	0.174	-	-	-	-	-	-	0.121
	Min.	-0.642	-0.594	-	-	-	-	-	-	-0.394

(Continues)

**TABLE A1** (Continued)

Active DOF		All DOF, coupled inflow	All DOF	Surge and pitch	Surge	Sway	Heave	Roll	Pitch	Yaw
Roll (°)	Max.	0.646	0.599	-	-	-	-	-	-	0.326
	Avg.	0.106	0.094	-	-	-	-	0.069	-	-
	RMS	0.025	0.029	-	-	-	-	0.044	-	-
Surge (m)	Min.	0.035	0.008	-	-	-	-	-0.032	-	-
	Max.	0.183	0.186	-	-	-	-	0.178	-	-
	Avg.	8.117	8.096	8.078	5.092	-	-	-	-	-
Sway (m)	RMS	1.559	1.583	1.571	0.755	-	-	-	-	-
	Min.	2.639	2.513	2.539	2.335	-	-	-	-	-
	Max.	13.400	13.570	13.490	7.740	-	-	-	-	-
Heave (m)	Avg.	-0.143	-0.115	-	-	-0.009	-	-	-	-
	RMS	0.046	0.054	-	-	0.045	-	-	-	-
	Min.	-0.275	-0.266	-	-	-0.130	-	-	-	-
Yaw (°)	Max.	-0.018	0.040	-	-	0.118	-	-	-	-
	Avg.	-0.180	-0.177	-	-	-	-0.072	-	-	-
	RMS	0.290	0.287	-	-	-	0.307	-	-	-
Pitch (°)	Min.	-1.105	-1.094	-	-	-	-1.065	-	-	-
	Max.	0.796	0.793	-	-	-	0.916	-	-	-

Note: Columns are organized by which platform degree of freedom is enabled for that case.

<sup>a</sup>The average power for an equivalent fixed-bottom turbine is 1.661 MW for coupled inflow cases and 1.605 MW for prerecorded inflow cases.

**TABLE A2** Semisubmersible data for time-averaged power for cases with the total floating displacements and average displacements only, as well as average, root-mean-square, minimum, and maximum values for rotor and platform displacements

Active DOF:		All DOF, coupled inflow	All DOF	Surge and pitch	Surge	Sway	Heave	Roll	Pitch	Yaw
Power (MW) <sup>a</sup>	Total disp.	1.664	1.608	1.604	1.630	1.606	1.607	1.606	1.694	1.606
	Avg. disp.	-	1.591	1.591	1.606	1.606	1.606	1.606	1.591	1.606
$x_{rc}$ (m)	Avg.	8.417	8.359	8.327	5.571	-	-	-	2.729	-
	RMS	1.218	1.214	1.148	1.459	-	-	-	2.583	-
	Min.	3.092	3.102	4.147	1.259	-	-	-	-5.270	-
	Max.	12.859	12.821	12.887	10.340	-	-	-	12.147	-
$y_{rc}$ (m)	Avg.	-0.205	-0.171	-	-	-0.010	-	-0.167	-	-
	RMS	0.062	0.072	-	-	0.038	-	0.024	-	-
	Min.	-0.373	-0.373	-	-	-0.110	-	-0.259	-	-
	Max.	-0.051	0.027	-	-	0.104	-	-0.077	-	-
$z_{rc}$ (m)	Avg.	-0.027	-0.026	-0.051	-	-	0.033	-	-0.079	-
	RMS	0.853	0.853	0.041	-	-	0.847	-	0.098	-
	Min.	-3.206	-3.205	-0.354	-	-	-3.014	-	-0.824	-
	Max.	3.027	3.027	-	-	-	3.028	-	-	-
$\phi_{rc}$ = Pitch (°)	Avg.	1.773	1.746	1.754	-	-	-	-	1.738	-
	RMS	0.761	0.759	0.780	-	-	-	-	1.646	-
	Min.	-0.570	-0.580	-1.106	-	-	-	-	-3.357	-
	Max.	4.911	4.840	5.083	-	-	-	-	7.757	-
$\theta_{rc}$ = Yaw (°)	Avg.	0.009	0.011	-	-	-	-	-	-	-0.006

(Continues)

**TABLE A2** (Continued)

Active DOF:		All DOF, coupled inflow	All DOF	Surge and pitch	Surge	Sway	Heave	Roll	Pitch	Yaw
	RMS	0.155	0.185	-	-	-	-	-	-	0.182
	Min.	-0.453	-0.526	-	-	-	-	-	-	-0.554
	Max.	0.607	0.713	-	-	-	-	-	-	0.668
Roll (°)	Avg.	0.113	0.105	-	-	-	-	0.106	-	-
	RMS	0.023	0.026	-	-	-	-	0.015	-	-
	Min.	0.024	0.011	-	-	-	-	0.049	-	-
	Max.	0.187	0.183	-	-	-	-	0.165	-	-
Surge (m)	Avg.	5.633	5.616	5.572	5.571	-	-	-	-	-
	RMS	1.364	1.363	1.373	1.459	-	-	-	-	-
	Min.	1.375	1.359	1.374	1.259	-	-	-	-	-
	Max.	10.180	10.200	10.110	10.340	-	-	-	-	-
Sway (m)	Avg.	-0.027	-0.006	-	-	-0.010	-	-	-	-
	RMS	0.047	0.056	-	-	0.038	-	-	-	-
	Min.	-0.129	-0.136	-	-	-0.110	-	-	-	-
	Max.	0.096	0.148	-	-	0.104	-	-	-	-
Heave (m)	Avg.	0.024	0.024	-	-	-	0.033	-	-	-
	RMS	0.849	0.849	-	-	-	0.847	-	-	-
	Min.	-3.147	-3.147	-	-	-	-3.014	-	-	-
	Max.	3.084	3.084	-	-	-	3.028	-	-	-

Note: Columns are organized by which platform degree of freedom is enabled for that case.

<sup>a</sup>The average power for an equivalent fixed-bottom turbine is 1.661 MW for coupled inflow cases and 1.605 MW for prerecorded inflow cases.